Urban Heat Risk Mapping Using Multiple Point Patterns in Houston, Texas

Jacob W. Mortensen

Department of Statistics, Brigham Young University, Provo, UT 84602, United States.

Dr. Matthew J. Heaton

Department of Statistics, Brigham Young University, Provo, UT 84602, United States.

Olga V. Wilhelmi

Research Applications Laboratory, National Center for Atmospheric Research, Box 80307-3000, Boulder, CO, United States.

Summary. Extreme heat, or persistently high temperatures in the form of heat waves, adversely impact human health. To study such effects, risk maps are a common epidemiological tool used to identify regions and populations that are more susceptible to these negative outcomes; however, the negative health effects of high temperatures are manifested differently among different segments of the population. In this paper, we propose a novel, hierarchical marked point process model that merges multiple health outcomes into an overall heat risk map. Specifically, we consider health outcomes of heat stress-related 911 calls and mortalities across the city of Houston, Texas. We show that combining multiple health outcomes leads to a broader understanding of the spatial distribution of heat risk than a single health outcome.

Keywords: Poisson point processes, risk mapping

1. Introduction

1.1. Research Motivation

Epidemiological evidence suggests that extreme or persistently high temperatures negatively impact public health. For example, Basu and Samet (2002), Gosling et al. (2009), Anderson and Bell (2011) and Gasparrini and Armstrong (2011) have found that elevated temperatures increase mortality. Similarly, empirical evidence suggests that increases in temperature are also related to increases in morbidity counts (Li et al., 2012), hospitalizations (Rusticucci et al., 2002; Schaffer et al., 2012) and ambulance dispatches (Ng et al., 2014). As recently as 2015, heat waves in India and Pakistan contributed to the deaths of hundreds of people (Mohsin and McKirdy, 2015). Studies by Luber and McGeehin (2008), Meehl and Tebaldi (2004), Nicholls (2009) and Peng et al. (2011) suggest that, due to climate change, such negative health outcomes are projected to increase in the future.

Risk (i.e. disease) mapping (Lawson, 2013) is a common technique used by epidemiologists to understand the spatial distribution of those adversely affected by heat. However, Wilhelmi and Hayden (2010), Wolf et al. (2010), Uejio et al. (2011) and Heaton (2014) argue that the impact of heat on health is a multifaceted phenomenon that affects different segments of a population in different ways. For example, heat may lead to mortality in some but dehydration in others. Thus, considering different health outcomes can lead to different risk maps, each of which captures only a small piece of the larger, cumulative impact of heat.

Consider, for example, the two sources of data displayed in Figure 1. Figure 1a displays a contour plot of a kernel density estimate of the locations to which ambulances were dispatched in 2054 heat-related emergency calls to 911 occuring between May and September 2006-2010 classified under at least one of the terms "heat," "dehydration," "heat exhaustion," or "heat stroke" (exact locations of the calls cannot be shown in order to preserve confidentiality). Figure 1b, however, displays a contour plot of the residences of 15,244 mortalities that occurred between May and September of the years 1999 through 2006 where the primary cause of death was connected to either cardiovascular or kidney

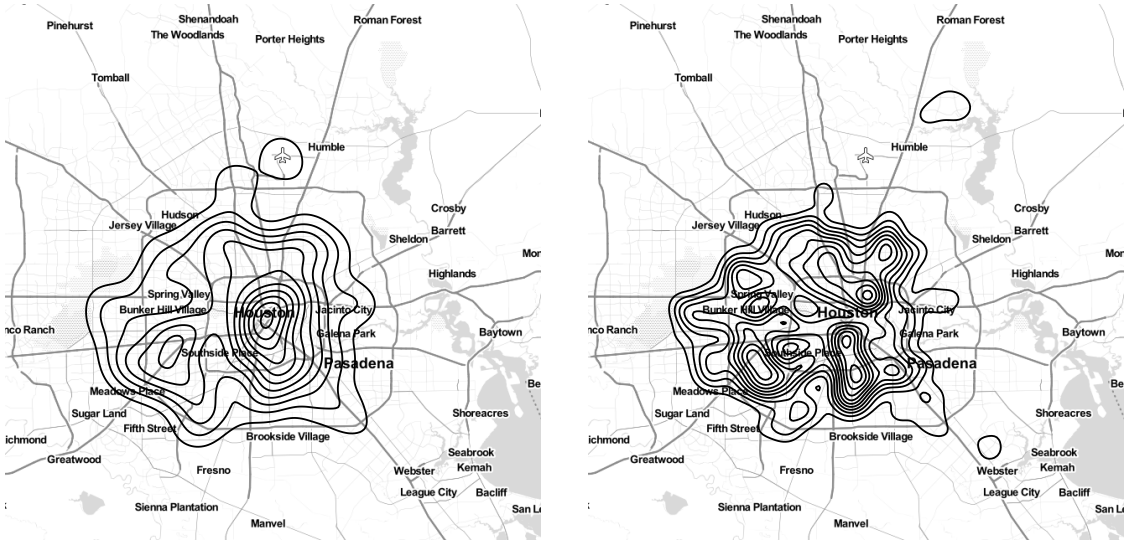

a) 911 Data b) Mortality Data

Fig. 1. Contour plots for kernel density estimates of the locations of heat-related 911 calls and mortalities. 911 call data courtesy of the Houston Fire Department. Mortality data courtesy of the Texas Department of State Health Services.

problems. Inevitably, some of the deaths in this group will not be directly heat-related, but both causes have been shown to have a strong relationship with heat (Kjellstrom et al., 2010).

Examination of the contour plots reveals that while the density of 911 calls is concentrated on a single location in the center of Houston, the density for the mortality data is more diffuse, exhibiting three distinct areas of concentration. The fact that the spatial distribution of heat-related 911 calls is different than that of heat-related mortalities suggests that each measure captures only part of the overall effects of heat on health. As a result, being able to combine the information contained in each of the different data sources into a single risk map in a systematic, model-based fashion becomes a useful tool in understanding how different areas in a city are impacted by extreme heat as opposed to a more narrow view of where a 911 call or mortality is most likely to take place.

1.2. Research Goals and Contributions

Motivated by the multifaceted impact of heat on health in Houston, we seek to model multiple health outcomes jointly and create a single, combined risk map for heat across Houston, TX. The basic tool that we employ to achieve this goal is a Poisson point process which we review briefly here; the interested reader is directed to Moller and Waagepetersen (2003), Gelfand et al. (2010), or Banerjee et al. (2014) for a more rigorous treatment. A *spatial* point process is a random process on a spatial domain $\mathcal{D}$ where realizations consist of a finite set of spatial locations $\mathcal{S} = \{\mathbf{s}_1, \ldots, \mathbf{s}_n : \mathbf{s}_i \in \mathcal{D} \; \forall \; i\}$. The distribution of $\mathcal{S}$ is governed by an intensity function $\Lambda(\mathbf{s}) : \mathcal{D} \rightarrow [0, \infty)$. The point process is said to be Poisson because for any subset $\mathcal{B} \subseteq \mathcal{D}$, $N(\mathcal{B})$, the random number of points falling in $\mathcal{B}$, is distributed $\mathcal{P}(\delta)$ where $\mathcal{P}(\delta)$ denotes the Poisson distribution with mean $\delta = \int_{\mathcal{B}} \Lambda(\mathbf{s}) d\mathbf{s}$. Further, the density of the realized set of locations $\mathcal{S}$ is given by the normalized intensity $\lambda(\mathbf{s}) = \Lambda(\mathbf{s}) / \int_{\mathcal{D}} \Lambda(\mathbf{s}) d\mathbf{s}$. In statistical analysis for point patterns, $\Lambda(\mathbf{s})$ is unknown. Hence, focus is on parameterizing, and subsequently estimating, $\Lambda(\mathbf{s})$.

Treating the heat-related 911 calls and mortalities as realizations of a point pattern,

we seek to parameterize two unknown intensity surfaces, say $\Lambda_1(\mathbf{s})$ and $\Lambda_2(\mathbf{s})$, where each surface represents a "risk map" such that regions where $\Lambda_1(\mathbf{s})$ (or $\Lambda_2(\mathbf{s})$) is high are regions where a heat stress-related 911 call or mortality is likely to occur. Examples using point pattern models as risk maps are prevalent and include Best et al. (2000), Chakraborty et al. (2011), Heaton (2014), and Heaton et al. (2015) to name only a few. The inherent difficulty with point process models lies in modelling the infinite-dimensional intensity surfaces, $\Lambda_1(\mathbf{s})$ and $\Lambda_2(\mathbf{s})$. Popular choices include a Gaussian process model for $\log(\Lambda_p(\mathbf{s}))$ (referred to as the Cox process; see **?**) but this results in difficulties in calculating the associated likelihood due to the presence of a random integral (Liang et al., 2009). A second option, is to make each $\Lambda_p(\mathbf{s})$ proportional to a closed-form density function (e.g. a normal mixture density; **?**) but specifying a sufficiently flexible density to capture the spatial variability in the Houston data would be difficult. Finally, a third option is to use a non-parametric density (**?**) but this presents similar computational challenges to the Cox process approach. In this article, we use principles from the Cox process approach but use a discretized intensity surface to overcome computational issues.

The majority of point process examples in the literature consider only a single health outcome. The primary goal of this article is to utilize information from heat-related 911 calls and mortalities to not only estimate risk maps from each health outcome individually, but to merge each individual map (that is, intensity surface) into a single risk map that portrays the spatial distribution of the cumulative risk. In this regard, our work is similar to Liang et al. (2009) who model multiple types of cancer but do not consider merging the individual risk maps. To merge multiple intensity surfaces, we first model each health outcome as a realization of a point pattern with a specific intensity function (e.g. $\Lambda_1(\mathbf{s})$ and $\Lambda_2(\mathbf{s})$). Then, hierarchically, these individual intensity functions are treated as random draws from a "cumulative" or "mean" intensity function that acts as a combined risk map for the city of Houston. By defining the risk maps in this hierarchical modeling framework, uncertainty associated with each intensity surface can be appropriately quantified.

Beyond the spatial distribution of the 911 calls and mortalities, it is also of epidemiological interest to compare demographics for each heat-related health outcome. For example,

the 911 call and mortality data sources also include the age, race/ethnicity, and gender of the respective individual. A secondary contribution of this research is estimating the differences in demographics among the various health outcomes. Therefore, we append the aforementioned point patterns also to include the intensity surfaces for the associated marks of age, gender and race/ethnicity. This allows for a model-based comparison of how heat affects subpopulations differently. Because each of the associated marks are discrete, we introduce a modeling framework that allows for conjugate updates of the associated non-spatial intensity surfaces.

In summary, there are three primary contributions of this research, two statistical and one epidemiological: (i) introduction of a computationally feasible, discrete parameterization of intensity surfaces for point pattern models, (ii) development of a hierarchical framework for merging multiple risk maps, and (iii) identifying differential risks to multiple health outcomes among subpopulations. The remainder of this paper is as follows: Section 2 outlines the statistical model we use to analyze the data and to produce the desired risk maps. Section 3 includes the generated risk maps for the 911 and mortality data and details the results. Finally, section 4 discusses the implications of our results and provides suggestions for future research.

2. Statistical Model

This section describes a hierarchical model for merging heat-related 911 calls and mortalities in order to estimate a cumulative risk map. The model is presented in terms of (i) the likelihood layer describing the distributional assumptions of the observed point patterns, (ii) the process layer describing how the two health outcomes are interrelated and, finally, (iii) the prior layer describing *a priori* assumptions of model parameters.

2.1. Likelihood Layer

Let $\mathbf{s}_{pi} \in \mathcal{D}$ be the latitude-longitude coordinate of the location for the i^{th} individual who experienced health outcome p where $i = 1, 2, \ldots, n_p$, $p = 1, 2, \ldots, P$, such that P is the

total number of health outcomes under consideration (in this article, $P = 2$), and n_p is the total number of individuals who experienced health outcome p. Likewise, let $a_{pi} \in \{0, 1, 2, \ldots, 113\}$ represent the age of the i^{th} individual who experienced health outcome p; $g_{pi} \in \{\text{female}, \text{male}\}$ represent the gender of individual i who experienced health outcome p; and $e_{pi} \in \{\text{Asian}, \text{Black}, \text{Hispanic}, \text{White}\}$ be the race/ethnicity of individual i who experienced health outcome p. The upper bound of 113 for age was chosen arbitrarily but, in our data, there were no individuals with an age greater than 113. For other applications, this upper bound may need to be adjusted to account for the possibility of older ages. Finally, define $\mathbf{z}_{pi} = (\mathbf{s}'_{pi}, a_{pi}, g_{pi}, e_{pi})' \in \mathcal{Z}$ to be the vector of realized spatial locations and marks.

As stated in Chapter 1, we model $\{\mathbf{z}_{pi}\}_{i=1}^{n_p}$ as a realization from a Poisson point process with unknown and nonuniform intensity surface $\Lambda_p(\mathbf{s}, a, g, e)$ for $p = \{1, \ldots, P\}$. We choose to factor

$$\Lambda_p(\mathbf{z}) = \Lambda_p(\mathbf{s}, a, g, e) = \delta_p \alpha_p(a) \gamma_p(g) \xi_p(e) \lambda_p(\mathbf{s}) \tag{1}$$

where δ_p is an unknown constant controlling the expected number of individuals who experience health outcome p; $\alpha_p(a)$ is the probability of an individual with health outcome p being of age a; $\gamma_p(g)$ is the probability of an individual with health outcome p being of gender g; and $\xi_p(e)$ is the probability of an individual with health outcome p being of ethnicity e. In contrast, because $\mathbf{s}$ is continuous, $\lambda_p(\mathbf{s})$ is the density at location $\mathbf{s}$ for health outcome p. Notably, the model in (1) not only defines a risk map for health outcome p across space (via $\lambda_p(\mathbf{s})$), but also does so for each of the marks age (via $\alpha_p(a)$), gender (via $\gamma_p(g)$) and ethnicity (via $\xi_p(e)$).

Inherent in the factorization in (1) is the assumption that the marks of age, gender, ethnicity and spatial location are separable. For example, (1) assumes that the ethnicity of an individual does not impact the location of an event with health outcome p. Given potential ethnic/racial segmentation across the city of Houston, this is a strong assumption. However, we make this assumption here because (i) the goal of this analysis centers on spatial risk mapping for all individuals in Houston so as to identify the most at-risk areas

of the city regardless of ethnicity, age, or gender and (ii) the ethnicity for the majority of individuals in the mortality and 911 call data are either black or white. Hence, assuming a separate risk map for each ethnicity would severely diminish the amount of data available to estimate the risk surface for the other ethnicities.

In order to maintain the interpretations provided above, it must be the case that each of α_p, γ_p, ξ_p and λ_p sum (or integrate as is the case for λ_p) to 1 over their respective domains. This constraint is easily enforced for α_p, γ_p and ξ_p because each is discrete; however, enforcing $\int_{\mathcal{D}} \lambda_p(\mathbf{s}) d\mathbf{s} = 1$ in a flexible modeling framework is more onerous. Rather than using an approximation as in Liang et al. (2009), we discretize the spatial domain $\mathcal{D}$ by dividing it into $K = 1428$ 1-km^2 grid cells. Using this discretization, we parameterize

$$\lambda_p(\mathbf{s}) = \sum_{k=1}^{K} \frac{\phi_{pk}}{|\mathcal{G}_k|} \mathbb{1}\left\{\mathbf{s} \in \mathcal{G}_k\right\}, \tag{2}$$

where $\sum_{k=1}^{K} \phi_{pk} = 1$, $\mathcal{G}_k$ is the set of locations belonging to the k^{th} grid cell, $|\mathcal{G}_k|$ is the area of grid cell k, and $\mathbb{1}\left\{\mathbf{s} \in \mathcal{G}_k\right\}$ is an indicator function. Standard calculations reveal that $\int_{\mathcal{D}} \lambda_p(\mathbf{s}) = 1$ provided that $\sum_{k=1}^{K} \phi_{pk} = 1$ which leads to the interpretation that ϕ_{pk} is the probability that an event with health outcome p occurs in grid cell k. We note that the choice of 1-km^2 grid cells to perform the discretization is somewhat arbitrary. However, a 1-km^2 resolution is sufficiently fine for our purposes. Additionally, the grid used in the discretization matches the grid cells associated with temperature measurements that will be used as covariates below (see section 3.1).

As stated above, ϕ_{pk} can be interpreted as the probability of an event of health outcome p occuring in grid cell k. Because this probability is surely largely driven by the population of grid cell k, we set $\phi_{pk} \propto E_{pk} \exp(\phi^{\star}_{pk})$ where E_{pk} is a known constant representing the expected number of incidents of health outcome p in grid cell k and the normalizing constant is simply $\sum_{k=1}^{K} E_{pk} \exp(\phi^{\star}_{pk})$. We use internal standardization (see Waller and Gotway, 2004, chapter 2) and calculate

$$E_{pk} = \frac{\sum_{k=1}^{K} N_{pk}}{\sum_{k=1}^{K} \text{Pop}_k} \times \text{Pop}_k \tag{3}$$

where N_{pk} is the number of incidents of health outcome p that occur in grid cell k and Pop_k is the population of grid cell k. The parameterization $\phi_{pk} \propto E_{pk} \exp(\phi^\star_{pk})$ provides an intuitive interpretation for $\phi^\star_{pk}$: Namely, $\phi^\star_{pk}$ denotes the log relative risk of grid cell k. When $\phi^\star_{pk} > 0$ then grid cell k is said to have an elevated risk of heat-related health outcome p. Likewise, when $\phi^\star_{pk} < 0$ then grid cell k is said to have a decreased risk of heat-related health outcome p.

The population data used to calculate E_{pk} was taken from the 2000 census. Over the area covered by our 1428 grid cells there are 1461 irregularly shaped census block groups. We handle the misalignment between the block groups and our grid cells using a method outlined by Brunsdon and Comber (2015). In this process we calculate the intersection between grid cells and census block groups and use this to calculate the proportion of a grid cell that lies within a block group. If a grid cell spans multiple census block groups, the intersection will be split between those groups; if the grid cell is entirely contained within a block group, then the intersection will just be the grid cell itself. Let $\mathcal{C}_i$ represent census block group i and denote the proportion ω_{ki} as

$$\omega_{ki} = \frac{|\mathcal{G}_k \cap \mathcal{C}_i|}{|\mathcal{C}_i|}.$$

In this equation $|\mathcal{G}_k \cap \mathcal{C}_i|$ represents the area of the intersection between grid cell k and block group i and $|\mathcal{C}_i|$ is the area of block group i. Defining CensPop_i as the population count in $\mathcal{C}_i$ allows us to approximate the population count within grid cell k as

$$\text{Pop}_k = \sum_{i=1}^{N} \omega_{ki} \cdot \text{CensPop}_i,$$

where N is the total number of census block groups that intersect with grid cell k. Therefore, population within a given block group is distributed among intersecting grid cells based on the proportion of the group contained within a given grid cell. One weakness of this method is that it assumes that the population within a census block group is distributed equally throughout that group, which is almost certainly not the case. Unfortunately, due to restrictions on census data, demographic information (which we use elsewhere in the model) is not available at a finer resolution. As a result, we feel this approach is justified

in order to keep all census data incorporated in the model on the same scale.

A potential solution to avoid realigning the census data to the grid cells is to let the census block groups equal the $\mathcal{G}_k$ denoted in (2) rather than the grid cells. However, the heat information used in this research (described in detail in Section 3.1) is provided at a 1-km^2 resolution and these grid cells were chosen to align exactly with the available heat data. Using the block groups in place of the grid cells would necessitate aligning the heat information to the census block group areas. Because heat is our primary variable of interest we prefer realigning the demographic information to the grid associated with the heat data as opposed to the alternative. Therefore, we proceed having aligned the population data as described.

Now let $\mathbf{Z}_p = \{\mathbf{z}_{pi}\}_{i=1}^{n_p}$ be the collection of observations for health outcome p and let $\boldsymbol{\theta}$ denote the collection of all unknown parameters in (1) and (2). Assuming $\mathbf{z}_{pi} \perp \mathbf{z}_{p'i'}$ for $p \neq p'$ conditional on the intensity surfaces (that is, independent observations), using the derivation in Section 8.4 of Banerjee et al. (2014), the likelihood for the above parameters is

$$\begin{aligned} f(\{\mathbf{Z}_p\} \mid \boldsymbol{\theta}) &= \prod_{p=1}^{P} \left[\exp\left(-\int_{\mathcal{Z}} \Lambda_p(\mathbf{z}) d\mathbf{x} \right) \prod_{i=1}^{n_p} \Lambda(\mathbf{z}_{ip}) \right] \\ &= \prod_{p=1}^{P} \left[\exp\left(-\delta_p\right) \delta_p^{n_p} \prod_{i=1}^{n_p} \alpha_p(a_{pi}) \gamma_p(g_{pi}) \xi_p(e_{pi}) \lambda_p(\mathbf{s}_{pi}) \right], \end{aligned} \tag{4}$$

where $\int_{\mathcal{Z}} \Lambda_p(\mathbf{z}) d\mathbf{z} = \delta_p$ because $\alpha_p(a)$, $\gamma_p(g)$, $\xi_p(e)$ and $\lambda_p(\mathbf{s})$ sum (or integrate) to 1.

2.2. Process Layer

At the process layer of the model, we wish to combine each of the relative risks $\{\phi_{pk}^\star\}$ into a single relative risk map for any heat-related health outcome. Let $\boldsymbol{\phi}_p^\star = (\phi_{p1}^\star, \ldots, \phi_{pk}^\star)'$ denote the vector of log relative risks for health outcome p across each of the K spatial grid cells. We assume, for $p = 1, \ldots, P$,

$$\boldsymbol{\phi}_p^\star \overset{ind}{\sim} \mathcal{N}\left(\boldsymbol{\mu}, \sigma_p^2 \mathbf{M}_p\right), \tag{5}$$

where $\boldsymbol{\mu} = (\mu_1, \ldots, \mu_K)'$ is the mean vector of log relative risks across all P health outcomes, σ_p^2 is the variance of health outcome p, and $\mathbf{M}_p$ is the covariance matrix arising from the Matèrn covariance function with smoothness parameter ν_p and decay parameter ψ_p. In other words, the i, j element of $\mathbf{M}_p$ is given by $M_{\nu_p}(\|\mathbf{s}_i^\star - \mathbf{s}_j^\star\| \mid \psi_p)$ where $\mathbf{s}_i^\star$ is the centroid of the i^{th} grid cell and $M(\cdot)$ is the Matérn covariance function. We note, here, that the traditional tool for enforcing spatial correlation among areal units (grid cells) is the conditional autoregressive (CAR) model; however, the CAR model is defined in terms of pairwise differences and is, hence, not "centered." Because we wish to estimate the mean of multiple log relative risks, we opt for the Matérn covariance model to enforce spatial correlation.

The vector $\boldsymbol{\mu}$ is of particular interest in our model because it represents the combination of information from many different sources of health data into a single measure of the overall relative risk of heat on health rather than just the impact of heat on one indicator. In spite of a common mean, in (5) we allow a separate variance parameter for each health outcome (σ_p^2). We make this decisions based primarily on the kernel density estimates in Figure 1 which show that the density of the 911 calls is more peaked (i.e. larger variance of density values).

The primary assumption we make in (5) is that the relative risk surfaces for each health outcome share a common, underlying risk surface that is constant with respect to time. Naturally, the assumption would be violated if there is temporal variability between the relative risk surface in 1999-2006 (the time window for the mortality data) and 2006-2010 (the time window for the 911 call data). Unfortunately, given the data available to us, our assumption of a time-invariant relative risk surface is not able to be evaluated. That is, we would need information on the relative risk of mortality between 2006-2010 to investigate any inherent differences in the surface between 1999-2006 and 2006-2010 (which we don't have). Likewise, we would need 911 call data for the years 1999-2006 to assess any temporal differences in the risk of a 911 call (which we also don't have). While the possibility of a time-varying risk surface would be interesting from an epidemiological perspective, we leave this for future work.

An additional implicit assumption with (5) is the independence assumption among the log relative risks for each health outcome given the overall, "cumulative" log relative risk surface $\boldsymbol{\mu}$. For the application considered here this assumption is likely to, approximately, hold because the time frame for the 911 call data is 2006-2010 while the time frame for the mortality data is 1999-2006 (a minimal overlap); however, in other applications independence may not hold. In such cases, a multivariate spatial model (see Genton and Kleiber (2015) for a discussion) could be used in place of (5). We note the possible benefit of modeling dependence between the log relative risks but we do not explore this option here.

Additionally, at the process layer of the model we assume

$$\boldsymbol{\mu} \sim \mathcal{N}(\mathbf{X}\boldsymbol{\beta}, \sigma_\mu^2 \mathbf{M}_\mu) \tag{6}$$

where $\mathbf{X}$ is a $K \times Q$ design matrix of covariates with associated coefficients $\boldsymbol{\beta}$, σ_μ^2 is a variance and $\mathbf{M}_\mu$ is a spatial correlation matrix implied by the Matérn correlation function with smoothness ν_μ and decay ψ_μ. The regression in (6) allows us to assess if covariates such as poverty, age, or urban temperature affect the height of the global intensity surface through inference on the parameters $\boldsymbol{\beta}$.

2.3. Hyperprior Layer

At the hyperior prior layer of the model, we outline our prior assumptions for the model parameters in Sections 2.1 and 2.2. Because $\boldsymbol{\alpha}_p = (\alpha_p(0), \ldots, \alpha_p(113))'$ are probabilities where $\sum_a \alpha_p(a) = 1$, we assume

$$\boldsymbol{\alpha}_p \sim \text{Dir}(\mathbf{1}_{113})$$

for all p where $\text{Dir}(\cdot)$ denotes the Dirichlet distribution and $\mathbf{1}_{113}$ is a 1×113 vector of ones. Note that for a symmetric Dirichlet distribution with a concentration parameter of 1 across M categories, its density function simplifies to

$$\frac{1}{C} \prod_{i=1}^{M} x_i^{1-1} = \frac{1}{C}, \tag{7}$$

where C is a constant. Therefore, assuming $\boldsymbol{\alpha}_p \sim \text{Dir}(\mathbf{1}_{113})$ is equivalent to applying a uniform prior to $\boldsymbol{\alpha}_p$, and it follows that it is non-informative. Further, if we let $f(\boldsymbol{\alpha}_p)$ and

$f(\boldsymbol{\alpha}_p \mid \mathbf{Z}_p)$ represent the prior and posterior distributions for α_p, respectively, and let $n_{p,a}$ be the number of people who experienced health outcome p at age a, then we can use the likelihood in (4) to show that the Dirichlet prior described for $\boldsymbol{\alpha}_p$ is conjugate:

$$\begin{aligned} f(\boldsymbol{\alpha}_p \mid \mathbf{Z}_p) &\propto \mathrm{f}(\boldsymbol{\alpha}_p) f(\mathbf{Z}_p \mid \boldsymbol{\Theta}) \\ &\propto \left[\prod_{a=0}^{113} (\alpha_p(a))^{1-1}\right] \left[\prod_{a=0}^{113} (\alpha_p(a))^{n_{p,a}}\right] \\ &= \prod_{a=0}^{113} (\alpha_p(a))^{(n_{p,a}+1)-1}. \end{aligned} \tag{8}$$

Stated explicitly, the posterior distribution of $\boldsymbol{\alpha}_p$ is a Dirichlet distribution with concentration parameters $(n_{p,0}+1, n_{p,1}+1, \ldots, n_{p,113}+1)$. In a similar vein, we assume

$$\boldsymbol{\gamma}_p = (\gamma_p(\text{female}), \gamma_p(\text{male}))' \sim \text{Dir}(\mathbf{1}_2)$$

and

$$\boldsymbol{\xi}_p = (\xi_p(\text{Asian}), \ldots, \xi_p(\text{White}))' \sim \text{Dir}(\mathbf{1}_4),$$

which, by the same argument, are also non-informative and conjugate priors.

Our approach for the remaining unknown parameters is to assume vague priors (and conjugate where possible). This is justified because there is sufficient data to learn these parameters without the need to rely heavily on prior information. For δ_p, we assume $\delta_p \sim \mathcal{G}(0.001, 0.001)$, where $\mathcal{G}(a, b)$ denotes the gamma distribution with shape a and rate b. Note that for δ_p the likelihood in (4) is proportional to

$$\exp(-\delta_p)\, \delta_p^{n_p},$$

the kernel of a Poisson distribution. Therefore, the gamma prior for δ_p is conjugate, producing a posterior distribution of $\mathcal{G}(n_p + 0.001, 1 + 0.001)$. We assume $\{\sigma_p^2\}$ and σ_μ^2 are independent $\mathcal{IG}(2.001, 1.001)$ random variables where $\mathcal{IG}(a, b)$ denotes the inverse-gamma distribution with scale a and rate b, a well-known conjugate prior for normal variance parameters. The $\mathcal{IG}(2.001, 1.001)$ distribution has a variance of 1000, providing sufficient flexibility for the data to accurately dictate the variances. For the regression coefficients we

assume that $\boldsymbol{\beta} \sim \mathcal{N}(0, 50\mathbf{I}_Q)$, leading to a Gaussian complete conditional for $\boldsymbol{\beta}$. Conjugate prior distributions for each spatial smoothness parameter (the ν's) and decay parameter (the ψ's) are not available; however, following the results of Zhang (2004), a vague prior for the variance parameters (the σ^2's) allows each smoothness and decay parameter to be fixed without loss generality or predictive power.

2.4. Model Fitting

Algorithm 1: Model fitting algorithm.

1 Let N be the number of MCMC draws, large enough that convergence is attained.
2 **for** p *in* $1:P$ **do**
3 Sample N draws from $\delta_p \sim \mathcal{G}(n_p + 0.001, 1.001)$;
4 Sample N draws from $\boldsymbol{\alpha}_p \sim \text{Dir}\left(n_{p,0}+1, n_{p,1}+1, \ldots, n_{p,113}+1\right)$;
5 Sample N draws from $\boldsymbol{\gamma}_p \sim \text{Dir}\left(n_{p,\text{Female}}+1, n_{p,\text{Male}}+1\right)$;
6 Sample N draws from $\boldsymbol{\xi}_p \sim \text{Dir}\left(n_{p,\text{Asian}}+1, \ldots, n_{p,\text{White}}\right)$;
7 **end**
8 **for** i *in* $1:N$ **do**
9 **for** p *in* $1:P$ **do**
10 Sample $\sigma_p^2 \sim \left[\sigma_p^2 | \boldsymbol{\phi}_p^\star, \mathbf{M}_p\right]$;
11 Sample $\boldsymbol{\phi}_p^\star \sim \left[\boldsymbol{\phi}_p^\star | \sigma_p^2, \mathbf{M}_p\right]$;
12 **end**
13 Sample $\sigma_\mu^2 \sim \left[\sigma_\mu^2 | \boldsymbol{\mu}, \boldsymbol{\beta}, \mathbf{M}_\mu\right]$;
14 Sample $\boldsymbol{\mu} \sim \left[\boldsymbol{\mu} | \{\boldsymbol{\phi}_p^\star\}, \{\sigma_p^2\}, \{\mathbf{M}_p\}, \sigma_\mu^2, \mathbf{M}_\mu, \boldsymbol{\beta}\right]$;
15 Sample $\boldsymbol{\beta} \sim \left[\boldsymbol{\beta} | \boldsymbol{\mu}, \sigma_\mu^2, \mathbf{M}_\mu\right]$;
16 **end**

We fit this model within a Bayesian framework, using the Markov Chain Monte Carlo (MCMC) algorithm outlined in Algorithm 1. Notice that because the parameters on lines 2-7 all have conjugate priors (as described in Section 2.3), their posterior densities are

completely known and all N draws can be taken simultaneously. Recall that $n_{p,0}$ denotes the number of people who experienced health outcome p at age 0, $n_{p,Female}$ indicates the number of females who experienced health outcome p, and so on.

The complete posterior densities for the remaining parameters are unknown and so we obtain draws from the posterior using the Metropolis within Gibbs sampler outlined on lines 8-16 of Algorithm 1. We use the notation $[\theta|\psi_1, \ldots, \psi_k]$ to represent the complete conditional for the parameter θ dependent on parameters $\psi_1, \ldots, \psi_k$. Note that for the parameter updates on lines 10, 13, and 15 the complete conditional distributions are

$$\sigma_p^2 \sim \mathcal{IG}\left(2.001 + \frac{K}{2}, 1.001 + \frac{1}{2}\boldsymbol{\phi}_p^{\star\prime}\mathbf{M}_p^{-1}\boldsymbol{\phi}_p^{\star}\right), \tag{9}$$

$$\sigma_\mu^2 \sim \mathcal{IG}\left(2.001 + \frac{K}{2}, 1.001 + \frac{1}{2}(\boldsymbol{\mu} - \mathbf{X}\boldsymbol{\beta})'\mathbf{M}_\mu^{-1}(\boldsymbol{\mu} - \mathbf{X}\boldsymbol{\beta})\right), \text{ and} \tag{10}$$

$$\boldsymbol{\beta} \sim \mathcal{N}\left(\sigma_\mu^{-2}\Sigma^\star\mathbf{X}'\mathbf{M}_\mu^{-1}\boldsymbol{\mu}, \Sigma^\star)\right), \tag{11}$$

where M_p and M_μ are defined as in (5) and (6) and where $\Sigma^\star = \left[\frac{1}{50}I_Q + \frac{1}{\sigma_\mu^2}\mathbf{X}'\mathbf{M}_\mu^{-1}\mathbf{X}\right]^{-1}$. Because these belong to known families they can be drawn from directly using a Gibbs update, but the complete conditional distributions in steps 11 and 14 are not known and require a Metropolis-Hastings (MH) update.

Using a sampler of this design, 10000 draws were taken from the posterior distributions for each of these parameters, after a burn-in of 10000.† In order to assess convergence, we examined traceplots for each of the parameters and used Monte Carlo standard error (MCSE). Jones et al. (2006) calculate MCSE by dividing the chains into batches and using each batch mean to calculate variance between batches. Small MCSE values occur only when the variance between batches is low (i.e., each batch is approximately equal), thereby providing evidence of convergence. We calculated MCSE using the `mcmcse` package in R (Flegal et al., 2015), and the largest MCSE value for all of our parameters was XXXXX. Based on these MCSE values and visual inspection of the traceplots, we are satisfied that convergence was attained.

†R code used to implement this algorithm is provided in the supplementary materials.

3. Results

3.1. Covariates and Variable Selection

In order to get heat information at the resolution necessary for this study, we used temperature data simulated using an offline version of the Noah Land Surface Model, known as the High Resolution Land Data Assimilation System (HRLDAS). These data consist of 15,625 HRLDAS 1-km^2 grid boxes that cover the Houston area and contain 6 temperature measurements that we consider: daily max/min temperature at 2 meters above the ground (T2), daily max/min NWS heat index (HI), and daily max/min Swedish wet-bulb-globe temperature (SWBG). To get a measure of the "heat" associated with locations across the city, the values for each of these variables were averaged across the months May through September of 1999 – 2010 (the time window for all observed health outcomes).

We fit the model in Section 2 using each of these temperature variables (one at a time) and then calculated the deviance information criterion (DIC) (Spiegelhalter et al., 2002) as a measure of model fit. Table 3.1 shows that the model produced the lowest DIC value when fit with max HI so the numerical estimates and risk maps shown in this chapter are from the model fit with this temperature measurement. Figure 2 displays the average maximum HI values associated with each grid cell and shows a clear spatial distribution, with higher temperatures concentrated near the city center. Note that the DIC values in Table 3.1 are all very close, indicating little difference in model fit between the different variables. This is, perhaps, due to the fact that the covariates enter our model at the mean intensity surface layer (in the regression for $\boldsymbol{\mu}$) at which point it is difficult to distinguish between the different heat variables. That is, because $\boldsymbol{\mu}$ captures both the 911 calls and mortalities, it is possible that any of the measured heat variables explain the combined impact of heat on "health" whereas specific heat variables better explain specific health outcomes.

Recall that in (6) $\boldsymbol{\mu}$ can be regressed on covariates $\mathbf{X}$ in order to account for potential confounding effects. For all models that we considered $\mathbf{X}$ included an intercept term and temperature data detailed above. Table 3.1 shows which additional demographic variables

Table 1. DIC values for models fit with different temperature measurements.

Temperature Measurement	DIC
HI Max	220474
HI Min	221016
T2 Max	220998
T2 Min	220999
SWBG Max	221008
SWBG Min	221021

were included in $\mathbf{X}$ as well as indicating whether or not two-way interaction terms were also included in each model. The DIC in the final column of the table indicates that Model X provides the best fit for the data, and so the rest of this paper refers to this model. The percentage of people without air conditioning was taken from the Harris County tax assessor parcel database while all remaining covariates were taken from 2000 U.S. Census Data. Both data sources were aligned with our discrete grid using the method described in Section 2.1.

3.2. Risk Maps

The maps in Figure 3 show the posterior estimates for $\boldsymbol{\phi}_p^\star$ where $p \in \{911, \text{Mort}\}$, the log relative risks for each health outcome, and $\boldsymbol{\mu}$, the vector of log relative risks averaged across all health outcomes. Notice that in Figure 3a, the map showing $\boldsymbol{\phi}_{911}^\star$, the majority of the high risk area is concentrated in the city center. This is in line with the temperature measurements depicted in Figure 2, which shows a concentration of higher temperatures in the middle of Houston. Additionally, the area of highest concentration occurs in a downtown location with several parks and other walkable destinations, which may be a potential explanation for why heat-related 911 calls occur with relatively high frequency in this area.

Table 2. In order to control for potential confounding effects, we compared 15 different models that included a varie interactions. The variables included in each model and whether or not interaction terms were considered is indic DIC in order to compare models and select the one that provides the best fit.

	Variables									
	% over 65	% under 5	% Black	% Hispanic	% w/o AC	% disabled	% living alone	% in poverty	Interactions	DIC
Model 01										12345
Model 02	X	X								12345
Model 03			X	X						220523
Model 04					X	X	X	X		220482
Model 05	X	X	X	X						220526
Model 06	X	X			X	X	X	X		220512
Model 07			X	X	X	X	X	X		220497
Model 08	X	X	X	X	X	X	X	X		220498
Model 09	X	X							X	220529
Model 10			X	X					X	220455
Model 11					X	X	X	X	X	220493
Model 12	X	X	X	X					X	220522
Model 13	X	X			X	X	X	X	X	12345
Model 14			X	X	X	X	X	X	X	12345
Model 15	X	X	X	X	X	X	X	X	X	12345

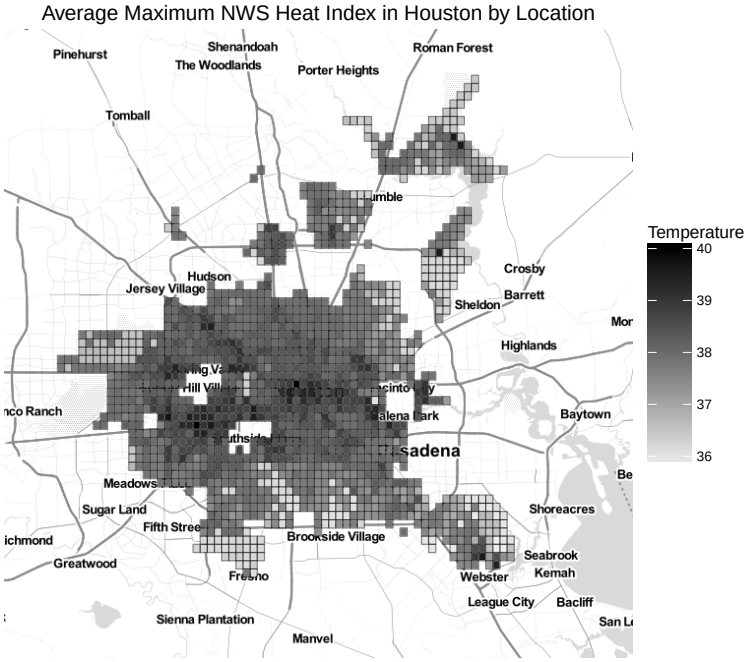

Fig. 2. Maximum NWS Heat Index in Houston, averaged over the summer months of 1999 – 2010. Notice that there is a clear concentration of higher temperatures in the center of the city.

There is a somewhat surprising area of extremely high relative risk for 911 calls in the northern part of the city; however, inspection of the underlying geography reveals that much of this area is covered by an airport, resulting in extremely low population levels (fewer than 25 people per square kilometer) yet a relatively large incidence of heat-related 911 calls (4, 6, and 7 phone calls in each of the three affected grid cells, respectively). Another important feature of the 911 call map is that the range for $\boldsymbol{\phi}^{\star}_{911}$ is much larger than the range for either $\boldsymbol{\phi}^{\star}_{\text{Mort}}$ or $\boldsymbol{\mu}$ and that far more of the $\boldsymbol{\phi}^{\star}_{911}$ values reach into the upper end of the distribution, with 7.4 percent of $\boldsymbol{\phi}^{\star}_{911}$ values greater than 1, compared to just 1.2 percent of the elements of $\boldsymbol{\phi}^{\star}_{\text{Mort}}$ greater than 1 and less than 1 percent of the elements of $\boldsymbol{\mu}$ greater than 1. This is likely due to sparsity of data: if more heat-related 911 calls were observed, the associated locations could potentially be more diffuse than those currently observed, leading to lower relative risk scores. Notice also that the credible interval widths (see Figure 3b), unsurprisingly, are largest where no 911 calls were observed and estimation of $\phi^{\star}_{911,k}$ was dependent entirely on spatial correlation.

The risk map depicting $\boldsymbol{\phi}^{\star}_{\text{Mort}}$ shown in Figure 3c also displays a concentration of high relative risk in the city center, but additionally shows a clear "Y"-shaped pattern extending from the middle of the city. Reasons for this difference in distribution are not immediately clear, although it is worth noting that the pattern roughly coincides with several arterial thoroughfares. This demonstrates a clear difference in the spatial distribution of heat-related mortalities when compared to the spatial distribution of the 911 calls. Due to the profusion of mortality data, the associated credible interval widths are much narrower than those for the 911 call data, although many of the intervals near the city periphery are still quite large.

Figure 3e shows the spatial distribution of $\boldsymbol{\mu}$ and again we see heavy concentration in the center of Houston. Notice that this surface appears to be much smoother than the other two and that the range of values is compressed in comparison to both of the other health outcomes, but that in general, the areas of higher relative risk for $\boldsymbol{\mu}$ reflect those seen in the other two maps. Examination of the correlations between the three relative risk surfaces showed that $\boldsymbol{\mu}$ was correlated most highly with $\boldsymbol{\phi}^{\star}_{\text{Mort}}$ ($r = 0.82$), and that

Table 3. β coefficients for variables. Because none of the credible intervals contain 0, we conclude that each variable has

Variable	β	95% HPD Credible Interval
Intercept	-26.378	$(-35.268, -15.397)$
Average Heat Index	0.622	$(0.356, 0.842)$
% Over 65	8.394	$(4.851, 12.237)$
No Air Conditioning	0.004	$(0.003, 0.006)$

the correlation with $\boldsymbol{\phi}^{\star}_{911}$, while still strong, was slightly lower ($r = 0.68$). In both cases, the correlation between $\boldsymbol{\mu}$ and each $\boldsymbol{\phi}^{\star}_{p}$ was much stronger than the correlation between $\boldsymbol{\phi}^{\star}_{911}$ and $\boldsymbol{\phi}^{\star}_{\text{Mort}}$ ($r = 0.54$), suggesting that this mean surface is successfully borrowing information from both data sources, and that although the mortality data might carry more weight (as there are far more observations), the phone call data is still providing valuable input in the estimation of $\boldsymbol{\mu}$.

In Table 2 we see the estimates for the $\boldsymbol{\beta}$ coefficients estimated as part of the mean of $\boldsymbol{\mu}$. None of the associated credible intervals contain zero, and so we conclude that each of the variables included in this mean has a statistically significant relationship with the average relative risk across all health outcomes. We see that each of the variables considered has a positive relationship with relative risk, and that as average heat index, percent of people in a grid cell over 65, and the number of people without central air conditioning in a grid cell all increase, so does the average relative risk. These effects come as no surprise: examination of the demographic variables in Section 3.3 shows that heat-related mortalities were much more likely to occur for people older than 65, and further, as our response variables are associated with extreme heat, it makes sense that as heat increases or the ability to mitigate the effects of heat decreases (fewer people with air conditioning) the incidence of negative health outcomes associated with increased levels of heat should also increase.

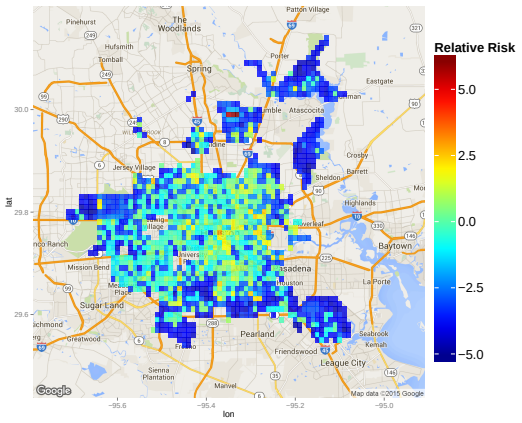

a) 911 Data

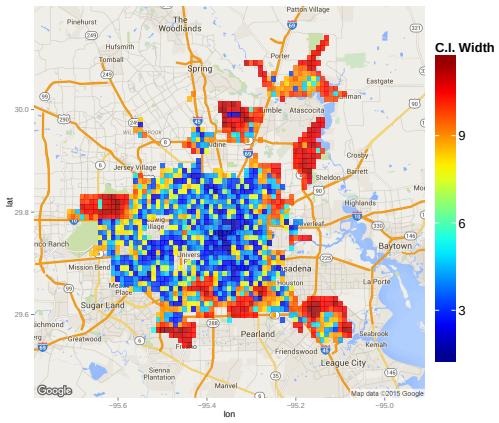

b) 95% CI Widths for 911 Data

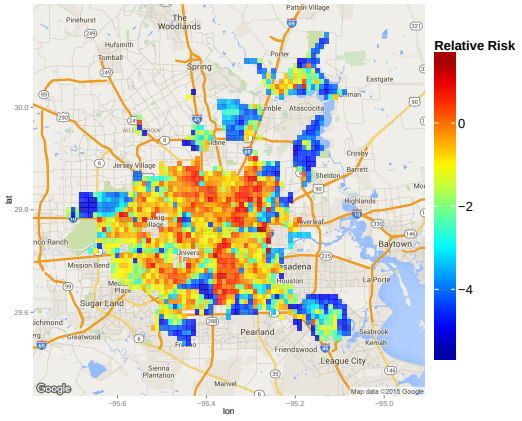

c) Mortality Data

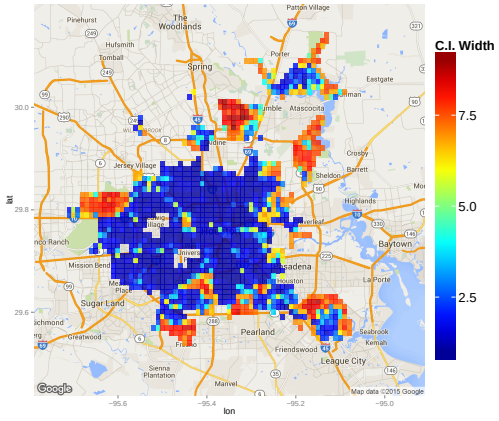

d) 95% CI Widths for Mortality Data

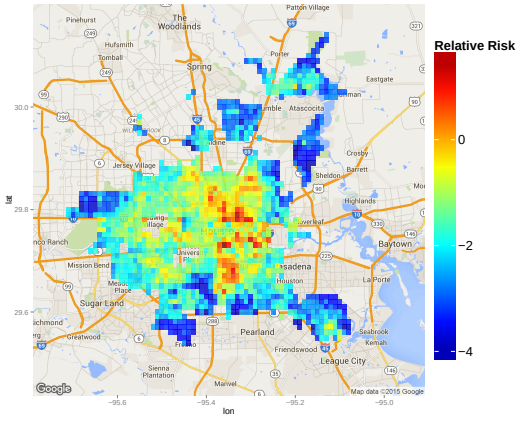

e) Overall

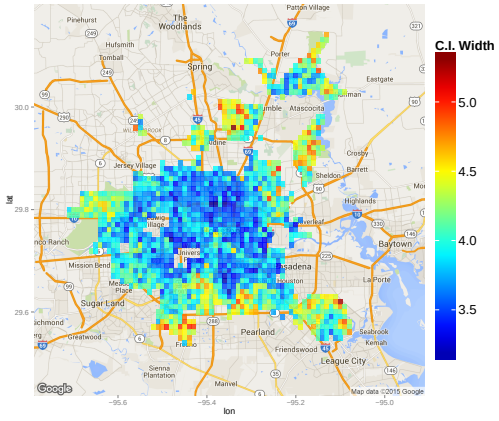

f) 95% CI Widths for Overall Relative Risk

Fig. 3. Log relative risk maps and 95% HPD credible interval (CI) widths for 911 calls, mortalities, and overall risk. The spatial distribution for the different health outcomes is obviously different, but the map of the overall relative risks shows evidence that information was successfully borrowed from both health outcomes.

3.3. Demographic Variables

Estimation of $\boldsymbol{\alpha}_p$, $\boldsymbol{\gamma}_p$, and $\boldsymbol{\xi}_p$ reveals some distinct differences between the subpopulations experiencing the two different health outcomes in our model. To begin with, Table 3 shows that while heat-related mortalities are slightly more likely to occur to females than males (0.51 versus 0.49), the probability of a heat-related 911 call occurring for a male is about 0.68 compared to a probability of just 0.32 for women. Examination of Table 4 reveals that population differences between the health outcomes are not limited to gender. The probabilities that a heat-related mortality occurs for an Asian, black, Hispanic or white individual are 0.02, 0.36, 0.11 and 0.5, respectively. Conversely, the comparable probabilities of a heat-related 911 call taking place are 0.02, 0.46, 0.26, and 0.27. Figure 5 shows that the probabilities for our last demographic variable, age, also differ greatly by health outcome, with the largest ξ_{911} values occurring between 25 and 50, compared with the largest ξ_{Mort} values clearly occurring above 75. We can also see that while it is extremely rare for a young child to experience a heat-related mortality the probability is much higher for 911 calls suggesting that while young children experience adverse effects from extreme heat they are unlikely to result in death.

Estimation of the effects of these demographic variables allows us to develop a profile for the type of person most likely to be impacted by extreme heat in a way that results in a specific health outcome. For example, we would expect heat-related mortalities to occur most often for white men and women older than 75 years while we expect heat-related 911 calls to occur most frequently for black males between 25 and 50 years old. These differences show that the effects of extreme heat are not uniform across a population and provide additional evidence that modeling multiple health outcomes, as we've done here, is a necessary step in understanding the total health impact of heat.

4. Conclusions

In conclusion, we successfully accomplished the stated goals of this research. Namely, we modeled the impact of heat on multiple health outcomes, calculating and mapping intensity

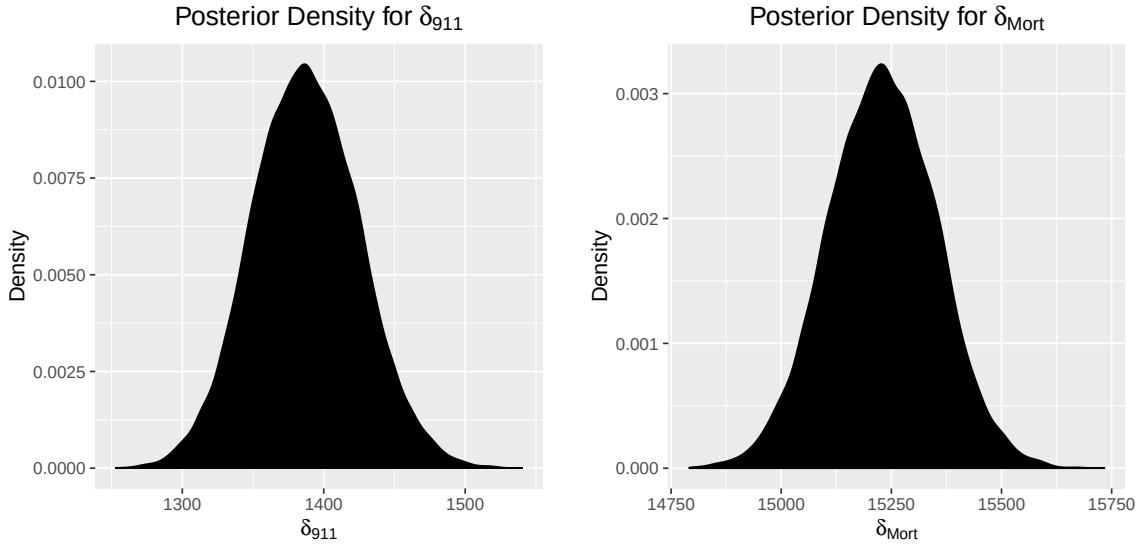

Fig. 4. Posterior density plots for δ_{911} and δ_{Mort}. The posterior mean for δ_{911} is 1387 and the posterior mean for δ_{Mort} is 15228

Table 4. Posterior probabilities and 95% HPD intervals for gender categories by health outcome. Notice that for that it occurred for a male is much higher than for a female whereas when looking at mortalities the probabilities for a male or female are nearly equal.

Gender				
	911 Calls		Mortalities	
	Value	95% HPD Int.	Value	95% HPD Int.
Female	0.316	(0.290, 0.343)	0.514	(0.506, 0.522)
Male	0.684	(0.657, 0.710)	0.486	(0.478, 0.494)

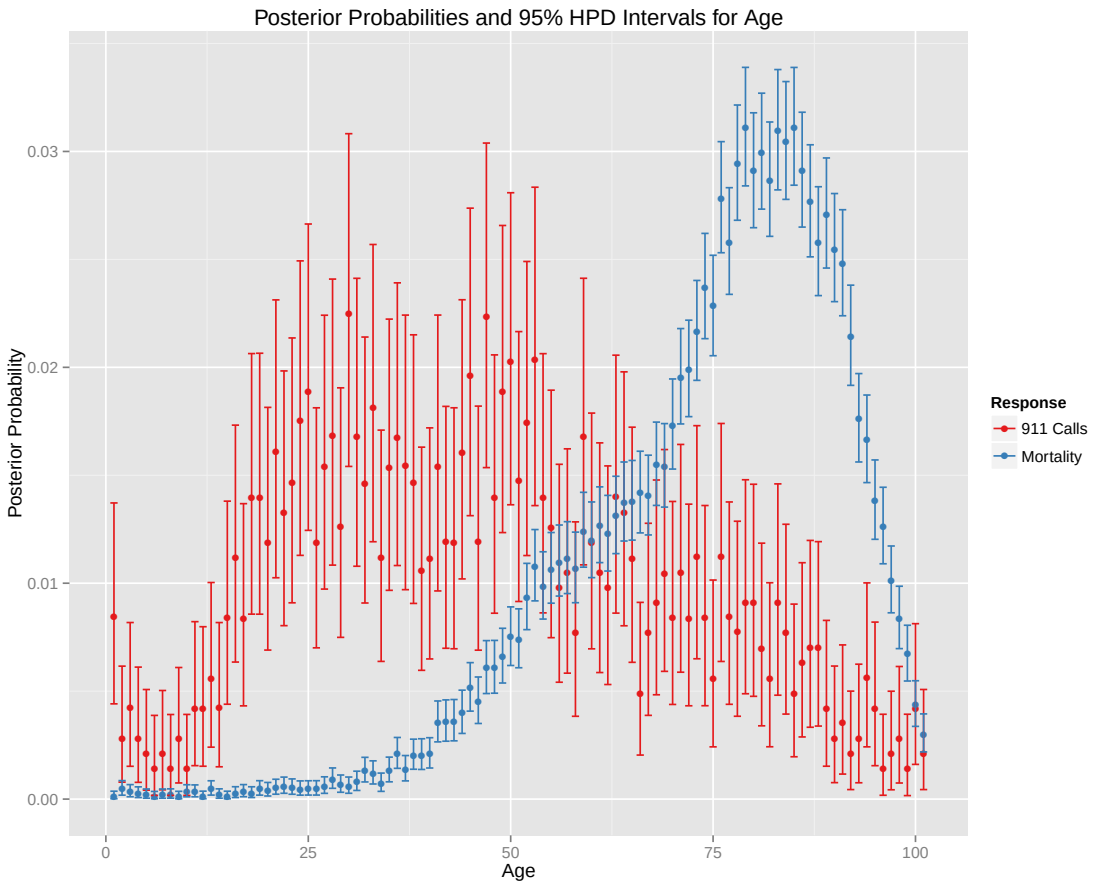

Fig. 5. Posterior probabilities and 95% HPD intervals associated with each age by health outcome. Notice that there are distinctly different patterns associated with the different health outcomes, again supporting the idea that it is necessary to consider multiple effects in order to understand the total impact of heat.

Table 5. Posterior probabilities and 95% HPD intervals for race/ethnicity categories by health outcome. Notice t
occur most frequently among the black population, mortalities occur most frequently among white people.

	Race/Ethnicity			
	911 Calls		Mortalities	
	Value	95% HPD Int.	Value	95% HPD Int.
Asian	0.020	(0.012, 0.028)	0.025	(0.022, 0.027)
Black	0.458	(0.429, 0.485)	0.361	(0.353, 0.369)
Hispanic	0.255	(0.231, 0.280)	0.114	(0.109, 0.119)
White	0.267	(0.241, 0.291)	0.501	(0.493, 0.509)

surfaces for each outcome individually as well as estimating and mapping the overall mean intensity surface. Our discretized approach to intensity surface modeling in Equation (2) provided a computationally simple approach that avoided calculation of a random integral. Examination of correlations showed that the mean intensity surface successfully borrowed information from both data sources and provides evidence that it is an accurate representation of the cumulative effect of heat. Further, we provided uncertainty estimates associated with each surface, allowing for greater precision when using these risk maps to make decisions about which areas are of greatest public health concern. While it has previously been possible to create a kind of overall risk map by simply aggregating data from various health outcomes, the ability to generate an overall risk map in a systematic, model-based fashion is a valuable contribution.

In addition to estimating the spatial effect of heat on health, we also estimated the probabilities of a health outcome occurring for specific demographic variables and showed distinct differences in how heat affected different subpopulations. These differences emphasize the significance of our research. By combining multiple health outcomes into a single model we are able to understand the impacts of heat in a way that is not captured by any single measure.

While this research includes interesting first steps towards effectively merging multiple

health outcomes, one issue not addressed herein (which is not well-addressed for all point process models) is the assessment of model goodness of fit. Other than post-hoc comparisons between maps of the observed data and maps of the intensity surfaces for the various health outcomes, there is no standard way to determine how well the model fits the data although work by **?**) suggests this is an active area of research. Another unaddressed issue is that throughout this analysis we treat temperature as fixed by using an average even though temperature is highly variable throughout the summer months. Initially, we attempted to incorporate distributed lag effects (Heaton and Peng, 2012) in this model but found that the data, especially the 911 call data, were too temporally sparse to estimate these effects well. Thus, developing an effective way to incorporate distributed lag effects and convert this from a purely spatial model to a spatial-temporal one is a potential avenue of further research.

The practical value of this research becomes apparent as public health officials seek to plan interventions to decrease the negative effects of extreme heat. Being able to consider and identify the areas that are most adversely affected across all negative health outcomes, instead of just one, can help to target resources in areas that are affected most heavily, leading to more effective and efficient responses to extreme heat.

References

Anderson, B. G. and Bell, M. L. (2011) Heat waves in the United States: Mortality risk during heat waves and effect modification by heat wave characteristics in 43 U.S. communities. *Environmental Health Perspectives*, **119**, 210–218.

Banerjee, S., Carlin, B. P. and Gelfand, A. E. (2014) *Hierarchical Modeling and Analysis for Spatial Data*. Boca Raton, FL: CRC Press, 2 edn.

Basu, R. and Samet, J. M. (2002) Relation between elevated ambient temperature and mortality: A review of the epidemiologic evidence. *Epidemiologic Reviews*, **24**, 190–202.

Best, N. G., Ickstadt, K. and Wolpert, R. L. (2000) Spatial Poisson Regression for Health

and Exposure Data Measured at Disparate Resolutions. *Journal of the American Statistical Association*, **95**, 1076–1088.

Brunsdon, C. and Comber, L. (2015) *An Introduction to R for Spatial Analysis and Mapping*. Thousand Oaks, CA: SAGE Publications Inc.

Chakraborty, A., Gelfand, A. E., Wilson, A. M. and Latimer, A. M. (2011) Point Pattern Modeling for Degraded Presence-Only Data over Large Regions. *Learning*, **60**, 1–28. URLhttp://onlinelibrary.wiley.com/doi/10.1111/j.1467-9876.2011.00769.x/full.

Flegal, J. M., Hughes, J. and Vats, D. (2015) mcmcse: Monte Carlo Standard Errors for MCMC.

Gasparrini, A. and Armstrong, B. (2011) The Impact of Heat Waves on Mortality. *Epidemiology*, **22**, 68–73.

Gelfand, A. E., Diggle, P. J., Fuentes, M. and Guttorp, P. (2010) *Handbook of Spatial Statistics*. Boca Raton, FL: CRC Press, 1 edn.

Genton, M. G. and Kleiber, W. (2015) Cross-Covariance Functions for Multivariate Geostatistics. *Statistical Science*, **30**, 147–163.

Gosling, S. N., Lowe, J. a., McGregor, G. R., Pelling, M. and Malamud, B. D. (2009) Associations between elevated atmospheric temperature and human mortality: A critical review of the literature. *Climatic Change*, **92**, 299–341.

Heaton, M. J. (2014) Wombling Analysis of Childhood Tumor Rates in Florida. *Statistics and Public Policy*, **1**, 60–67. URLhttp://www.tandfonline.com/doi/abs/10.1080/2330443X.2014.913512.

Heaton, M. J. and Peng, R. D. (2012) Flexible Distributed Lag Models Using Random Functions With Application to Estimating Mortality Displacement From Heat-Related Deaths. *Journal of Agricultural, Biological, and Environmental Statistics*, **17**, 313–331.

Heaton, M. J., Sain, S. R., Monaghan, A. J., Wilhelmi, O. V. and Hayden, M. H. (2015) An Analysis of an Incomplete Marked Point Pattern of Heat-Related 911 Calls. *Journal of the American Statistical Association*, **110**, 123–135. URLhttp://www.tandfonline.com/doi/full/10.1080/01621459.2014.983229.

Jones, G. L., Haran, M., Caffo, B. S. and Neath, R. (2006) Fixed-Width Output Analysis for Markov Chain Monte Carlo. *Journal of the American Statistical Association*, **101**, 1537–1547.

Kjellstrom, T., Butler, A. J., Lucas, R. M. and Bonita, R. (2010) Public health impact of global heating due to climate change: potential effects on chronic non-communicable diseases. *International journal of public health*, **55**, 97–103.

Lawson, A. B. (2013) *Bayesian Disease Mapping: Hierarchical Modeling in Spatial Epidemiology*. Boca Raton, FL: CRC Press, 2 edn.

Li, B., Sain, S., Mearns, L. O., Anderson, H. A., Kovats, S., Ebi, K. L., Bekkedal, M. Y. V., Kanarek, M. S. and Patz, J. A. (2012) The impact of extreme heat on morbidity in Milwaukee, Wisconsin. *Climatic Change*, **110**, 959–976.

Liang, S., Carlin, B. P. and Gelfand, A. E. (2009) Analysis of Minnesota colon and rectum cancer point patterns with spatial and nonspatial covariate information. *Annals of Applied Statistics*, **3**, 943–962.

Luber, G. and McGeehin, M. (2008) Climate Change and Extreme Heat Events. *American Journal of Preventive Medicine*, **35**, 429–435.

Meehl, G. a. and Tebaldi, C. (2004) More intense, more frequent, and longer lasting heat waves in the 21st century. *Science (New York, N.Y.)*, **305**, 994–997.

Mohsin, S. and McKirdy, E. (2015) Karachi heat wave: Unforgiving heat claims more lives. URLhttp://www.cnn.com/2015/06/25/asia/pakistan-heat-wave/.

Moller, J. and Waagepetersen, R. P. (2003) *Statistical Inference and Simulation for Spatial Point Processes*. Boca Raton, FL: CRC Press, 1 edn.

Ng, C. F. S., Ueda, K., Ono, M., Nitta, H. and Takami, A. (2014) Characterizing the effect of summer temperature on heatstroke-related emergency ambulance dispatches in the Kanto area of Japan. *International Journal of Biometeorology*, **58**, 941–948.

Nicholls, N. (2009) Estimating changes in mortality due to climate change. *Climatic Change*, **97**, 313–320.

Peng, R. D., Bobb, J. F., Tebaldi, C., McDaniel, L., Bell, M. L. and Dominici, F. (2011) Toward a quantitative estimate of future heat wave mortality under global climate change. *Environmental Health Perspectives*, **119**, 701–706.

Rusticucci, M., Bettolli, M. L. and De Los Angeles Harris, M. (2002) Association between weather conditions and the number of patients at the emergency room in an Argentine hospital. *International Journal of Biometeorology*, **46**, 42–51.

Schaffer, A., Muscatello, D., Broome, R., Corbett, S. and Smith, W. (2012) Emergency department visits, ambulance calls, and mortality associated with an exceptional heat wave in Sydney, Australia, 2011: a time-series analysis. *Environmental Health*, **11**, 3. URLhttp://www.pubmedcentral.nih.gov/articlerender.fcgi?artid=3292446{\&}tool=pmcentrez{\&}rendertype=abstract.

Spiegelhalter, D. J., Best, N. G., Carlin, B. P. and van der Linde, A. (2002) Bayesian Measures of Model Complexity and Fit. *Journal of the Royal Statistical Society Series B*, **64**, 583–639.

Uejio, C. K., Wilhelmi, O. V., Golden, J. S., Mills, D. M., Gulino, S. P. and Samenow, J. P. (2011) Intra-urban societal vulnerability to extreme heat: The role of heat exposure and the built environment, socioeconomics, and neighborhood stability. *Health and Place*, **17**, 498–507.

Waller, L. A. and Gotway, C. A. (2004) *Applied Spatial Statistics for Public Health Data*. Hoboken, NJ: John Wiley & Sons, Inc.

Wilhelmi, O. V. and Hayden, M. H. (2010) Connecting people and place: a new framework for reducing urban vulnerability to extreme heat. *Environmental Research Letters*, **5**, 014021.

Wolf, J., Adger, W. N., Lorenzoni, I., Abrahamson, V. and Raine, R. (2010) Social capital, individual responses to heat waves and climate change adaptation: An empirical study of two UK cities. *Global Environmental Change*, **20**, 44–52.

Zhang, H. (2004) Inconsistent Estimation and Asymptotically Equal Interpolations in Model-Based Geostatistics. *Journal of the American Statistical Association*, **99**, 250–261.